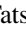


## Neutron capture cross section and capture $\gamma$ -ray spectrum of $^{88}\text{Sr}$ in the stellar nucleosynthesis energy region

Tatsuya Katabuchi <sup>\*</sup>, Masayuki Igashira, So Kamada,<sup>†</sup> and Michihide Tajika

*Laboratory for Zero-Carbon Energy, Tokyo Institute of Technology, 2-12-1, Ookayama, Meguro-ku, Tokyo 152-8550, Japan*

Nobuyuki Iwamoto

*Japan Atomic Energy Agency, 2-4 Shirakata Shirane, Tokai, Ibaraki 319-1195, Japan*

Toshihiko Kawano 

*Theoretical Division, Los Alamos National Laboratory, Los Alamos, New Mexico 87545, USA*



(Received 3 June 2022; accepted 8 August 2023; published 11 September 2023)

The neutron capture cross section and the capture  $\gamma$ -ray spectrum of  $^{88}\text{Sr}$  were measured in the keV energy regions: 10–89 keV and 510 keV. Between 34 and 89 keV, the present data are larger than evaluated cross sections which are based on a set of resonance parameters measured in past experiments. To investigate the impact of the present results to the stellar nucleosynthesis, the Maxwellian-averaged neutron capture cross section (MACS) was calculated using the present experimental results. The calculated MACS were about 10% smaller than the values from a previous work [Koehler *et al.*, *Phys. Rev. C* **62**, 055803 (2000)]. On the other hand, the present and previous MACS become in good agreement when the contribution from the direct neutron capture process that has been theoretically calculated is removed from the previous MACS. This suggests that the previous work might overestimate the contribution of the direct capture process. The present experimental capture  $\gamma$ -ray spectrum shows that primary transition intensities to the low-lying states of  $^{89}\text{Sr}$  drastically change with the neutron energy. The ratio between the ground and first excited state transitions was compared with estimation derived from the resonance parameters and theoretical prompt  $\gamma$ -ray spectrum from the (*IJ*) neutron capture states. The estimation disagrees with the experimental values between 34 and 89 keV. This disagreement suggests that there are missed or (*IJ*)-misassigned resonances in the previous resonance analysis.

DOI: [10.1103/PhysRevC.108.034610](https://doi.org/10.1103/PhysRevC.108.034610)

### I. INTRODUCTION

In the modern model of stellar nucleosynthesis, the slow neutron capture process (*s* process) is more complicated than was thought to be before [1]. In the *s*-process model, the elements from Fe to Zr ( $A \leq 90$ ) are created by the so-called weak component, which is driven by neutrons produced through the  $^{22}\text{Ne}(\alpha, n)^{25}\text{Mg}$  reaction in massive stars. The current stellar model suggests that the neutron production for the weak *s*-process occurs in two different burning stages, which are the He core burning and the following shell C burning [2,3]. In addition, the burning temperatures of the two stages are different,  $3 \times 10^8$  K for the He core burning and  $1 \times 10^9$  K for the shell C burning. Thus, a stellar model calculation to describe the weak *s* process requires accurate and reliable Maxwellian-averaged cross sections (MACS), not only at temperature  $kT = 25$  keV ( $3 \times 10^8$  K) but also at  $kT = 90$  keV ( $1 \times 10^9$  K). Pignatari *et al.* presented nucleosynthesis calculations for the stellar model using the

updated nuclear data and demonstrated that improvement in the MACS data significantly changed the prediction of isotope production yields in the *s* process. They concluded that more improvement in the experimental data for MACS calculation is necessary, especially at the higher temperatures for the shell C burning [4].

Strontium-88 has a small (*n,  $\gamma$* ) cross section due to its closed neutron shell structure. It becomes a bottleneck isotope in the *s*-process nuclear reaction network path. The  $^{88}\text{Sr}(n, \gamma)^{89}\text{Sr}$  cross section in the nucleosynthesis energy region is mainly described by the resolved neutron resonances. Koehler *et al.* has determined the resonance parameters from both capture and transmission measurements with the neutron time-of-flight (TOF) method at the Oak Ridge Electron Linear Accelerator (ORELA) [5,6]. Owing to long neutron flight paths (40, 80, and 200 m) of the ORELA beam lines, high resolution resonance measurements were achieved. The results had smaller uncertainties than previous measurement [7] and greatly improved the resonance parameters of  $^{88}\text{Sr}$ . They calculated the MACS using the experimental results, which agreed with values by the activation method [8]. Their resonance parameters were adopted in evaluated nuclear data libraries such as ENDF/B-VII.1 [9] and JENDL-4.0 [10]. However the firmness of the (*IJ*) assignments of

<sup>\*</sup>buchi@zc.iir.titech.ac.jp

<sup>†</sup>Present address: National Maritime Research Institute, 6-38-1, Shinkawa, Mitaka-shi, Tokyo 181-0004, Japan.

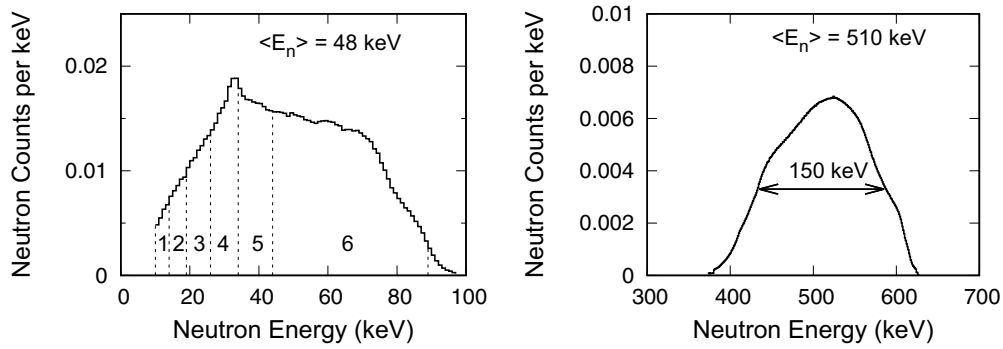


FIG. 1. Incident neutron spectra for the low energy (left) and the high energy (right) experiments. Neutron energy regions for analysis are shown as Gate 1 to 6 in the low energy spectrum. The average neutron energies were 48 keV and 510 keV. The spectra are normalized by the total area.

observed resonances were not satisfactory except for the  $s$ -wave resonances. Their statistical tests of obtained resonance parameters indicated that substantial numbers of  $p_{1/2}$  and  $p_{3/2}$  resonances could be missed or spuriously assigned.

This motivated us to carry out new measurements by a different type of experimental apparatus at the Tokyo Institute of Technology (Tokyo Tech). In this work, neutron capture  $\gamma$  rays from the  $^{88}\text{Sr}(n, \gamma)^{89}\text{Sr}$  reaction were measured with a heavily shielded NaI(Tl) spectrometer. The TOF method was employed with shorter neutron flight lengths (0.12 and 0.20 m) than ORELA. While the time resolution of the apparatus is poorer due to its short flight lengths, measurement of a smaller cross section can be achieved by the low background detection system [11]. In addition, using the NaI(Tl) detector, a neutron capture  $\gamma$ -ray spectrum, which gives more information on reaction mechanism, can be obtained. Preliminary results were reported in Ref. [12]. In the present paper, we finalized data analysis of the cross section and capture  $\gamma$ -ray spectrum, calculated MACS from the experimental cross section, and discussed the  $\gamma$ -ray spectrum comparing theoretical calculations.

## II. EXPERIMENTS AND DATA ANALYSIS

The experimental detail was described in Ref. [12]. Experiments were performed at the Laboratory for Zero-Carbon Energy of Tokyo Tech. A pulsed neutron beam was produced via the  $^7\text{Li}(p, n)^7\text{Be}$  reaction using a pulsed proton beam from a 3-MV Pelletron accelerator. The pulse width was 1.5 ns and the beam pulse cycle was 4 MHz. An isotopically enriched  $^{88}\text{Sr}$  sample (99.9% enrichment) in chemical form of  $\text{SrCO}_3$  was irradiated with neutrons. The net weight of  $^{88}\text{Sr}$  was 4.98 g. The  $\text{SrCO}_3$  powder was cased in a flat graphite container with an inner diameter of 55 mm. The thickness of the sample was 4.2 mm. A gold sample having the same diameter was also used for standard measurements. The weight of the Au sample was 46.2 g. Measurements were made in the two neutron energy regions: 10–89 keV and 510 keV. The incident neutron spectra were measured by the TOF method with two  $^6\text{Li}$  glass scintillation detectors. The flight path lengths to the  $^6\text{Li}$  glass detectors were 300 mm and 4.59 m for the low and high energy experiments, respectively. The incident neutron spectra are shown in Fig. 1. The full width at half-maximum

(FWHM) of the neutron energy distribution in the high energy experiment ( $E_n = 510\text{ keV}$ ) was 150 keV. Neutron capture  $\gamma$  rays from the sample were detected with a cylindrical NaI(Tl) detector (152.4 mm diam.  $\times$  304.8 mm long) surrounded by an annular NaI(Tl) detector for Compton suppression [13]. The detection angle of  $\gamma$  rays with respect to the neutron beam axis was  $125^\circ$ . The flight length from the neutron source to the sample was 120 mm for the low energy experiments and 200 mm for the high energy ones.

The detail of the data analysis procedure can be found elsewhere [14]. The TOF and the pulse height (PH) of detected events with the NaI(Tl) detector were sequentially recorded as two-dimensional data. Figure 2 shows a representative two-dimensional plot of TOF vs. PH for the low energy experiment. In TOF measurement, the 4-MHz signal from a proton beam pulse monitor was used as a stop signal of a time-to-amplitude converter because the 4-MHz signal overwhelms the system processing capacity when used as the TOF start trigger. Instead, the NaI(Tl) detector signal, which is at an acceptably low counting rate of  $\sim$ kcps, was fed into the time-to-amplitude converter as the start trigger. Hence, the  $x$  axis goes to larger channels as TOF becomes smaller in Fig. 2. A projection of the two-dimensional plot to the  $x$  axis

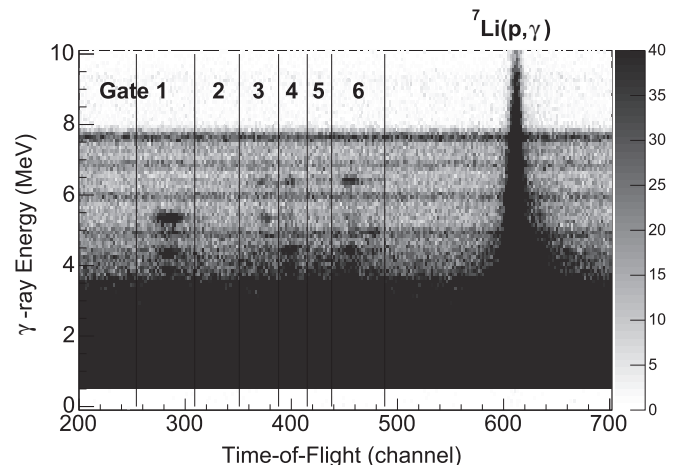


FIG. 2. Two-dimensional plot of time of flight vs. pulse height of the low energy experiments ( $E_n = 10\text{--}89\text{ keV}$ ).

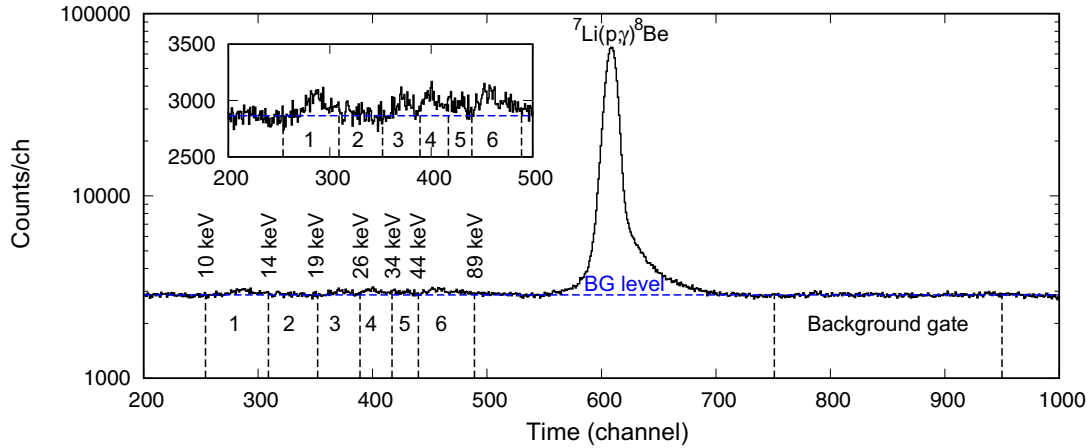


FIG. 3. TOF spectrum created by projecting the two-dimensional plot of Fig. 2 to the  $x$  axis. The TOF becomes smaller as the time channel goes larger. The time channel bin width is 0.245 ns. The six foreground and one background (BG) gates are also shown. The BG level determined from the BG gate is indicated as a blue dashed line. The inset is a close-up of the TOF region of neutron capture events in the  $^{88}\text{Sr}$  sample.

is shown in Fig. 3. The prominent peak around 600 channel is strong  $\gamma$ -ray events created in the  $^7\text{Li}(p, \gamma)^8\text{Be}$  reaction in the neutron source at  $t = 0$ . The  $(p, \gamma)$  peak channel is used as reference to calculate TOF. Time difference from the  $(p, \gamma)$  peak channel corresponds to TOF. The neutron capture events in the sample distribute below 500 channel. The background level shown as a dashed line was estimated from the background TOF gate (750–950 ch) where the direct neutrons from the neutron source did not exist. The close-up plot of Fig. 3 shows large count fluctuations caused by resonances of  $^{88}\text{Sr}$ . To take into account the resonance structure, six TOF gates were set for analysis. The gate energies are summarized in Table I. The bin widths ( $\Delta T$ ) of the TOF gates were chosen to be larger than the system time resolution ( $\approx 3$  ns). The numbers of reported resonances in Ref. [15] in the TOF gates are also given in Table I. For data analysis of the high energy experiment, one TOF gate was set around 510 keV.

The PH spectrum for each TOF gate was created by sorting the two-dimensional data with the TOF gates. The background

PH spectrum was constructed from events in the background TOF gate. Figure 4 shows background subtraction for Gate 3 as an example. As shown in Fig. 4(a), the background consists of mainly natural background ( $^{40}\text{K}$ ), and the neutron capture  $\gamma$  rays from  $^1\text{H}(n, \gamma)^2\text{H}$  and  $^{56}\text{Fe}(n, \gamma)^{57}\text{Fe}$  that were caused by the absorption of moderated thermal neutrons by material around the detector system. The counting rate of the background is constant, i.e., the count is proportional to duration of time. Thus, the background PH spectrum scaled by the ratio of the gate TOF period of the foreground to that of the background was subtracted from the foreground PH spectrum. The foreground and scaled background PH spectra are shown in Fig. 4(a). Figure 4(b) shows the net PH spectra after the background subtraction. The background was removed successfully and disappeared in the net PH spectrum.

The net PH spectra were unfolded with the detector response matrix using the unfolding code FERDOR [16]. The unfolded  $\gamma$ -ray spectra are shown in Figs. 5 and 6. The bars on top of the spectra indicate  $\gamma$ -ray energy positions

TABLE I. Neutron energies of the present measurements (low energy experiment) and the number of reported resonances [15] in the energy regions.

Gate	$E_n$ [keV]	$\Delta T$ [ns]	$L = 0$			$L = 1$			Major resonances (keV), $g\Gamma_n\Gamma_\gamma/\Gamma > 50$ meV
			$J = 1/2^+$	$1/2^-$	$3/2^-$	$1/2^-$	$3/2^-$		
1	10–14	13.5	1	2	0			$J = 1/2^+$ 13.84 $J = 1/2^-$ 12.41	
2	14–19	10.3	0	0	1			$J = 1/2^-$ 20.81 $J = 3/2^-$ 23.61	
3	19–26	9.1	0	1	1			$J = 1/2^-$ 29.52 $J = 3/2^-$ 29.52	
4	26–34	6.9	0	1	1			$J = 1/2^-$ 36.78, 39.07, 40.15 $J = 1/2^+$ 48.57	
5	34–44	5.6	0	3	0			$J = 1/2^-$ 46.47, 53.79, 55.95, 65.48 $J = 3/2^-$ 47.95, 54.66, 56.99, 73.77, 75.5, 76.89, 88.56	
6	44–89	12.3	2	4	7				

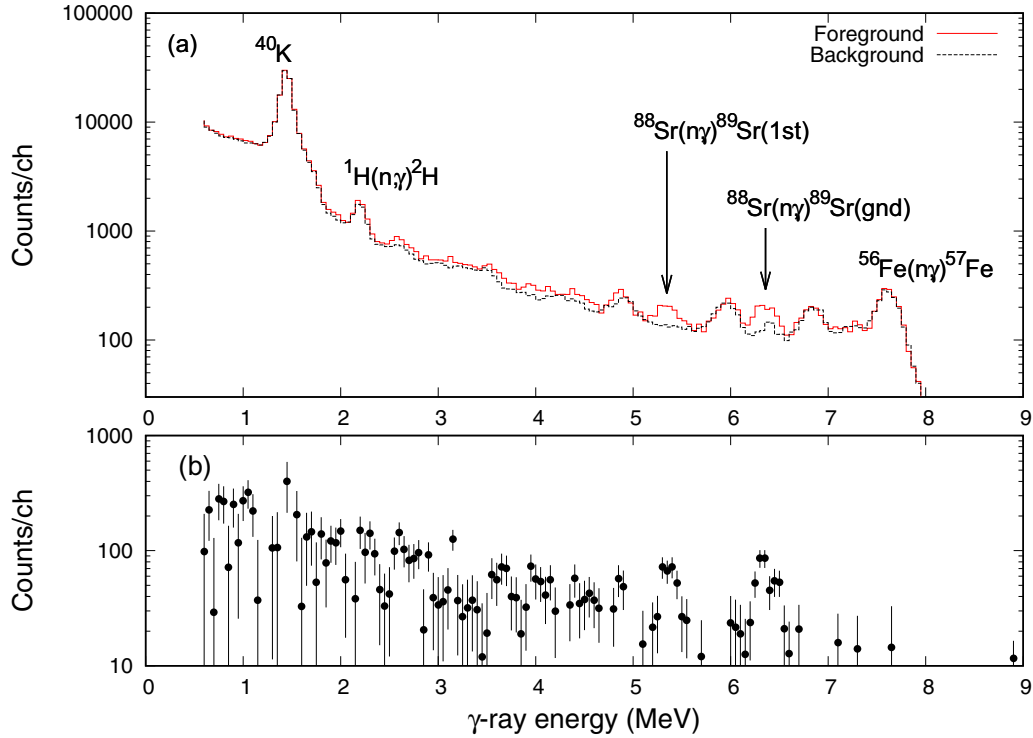


FIG. 4. (a) Foreground and background PH spectra. The foreground spectrum for TOF Gate 3 is shown as an example. The background spectrum was obtained from the background gate shown in Fig. 3. (b) Net PH spectrum of Gate 3 by subtracting the background from the foreground PH spectrum.

corresponding to primary transitions to known discrete levels of  $^{89}\text{Sr}$  in the database RIPL-3 [17]. The  $\gamma$ -ray spectra were normalized to satisfy the following equation:

$$\int_0^{B_n + E_{n.c.m.}} E_\gamma \nu(E_\gamma) dE_\gamma = B_n + E_{n.c.m.}, \quad (1)$$

where  $E_\gamma$  is the  $\gamma$ -ray energy,  $\nu(E_\gamma)$  is a normalized  $\gamma$ -ray spectrum,  $B_n$  is the neutron binding energy of  $^{89}\text{Sr}$  and  $E_{n.c.m.}$  is the neutron energy in the center-of-mass (c.m.) system. It is found that the primary transition pattern to low-lying states of the residual nucleus  $^{89}\text{Sr}$  drastically changes with the incident neutron energy. The  $\gamma$ -ray multiplicities above the detection threshold energy (600 keV) were calculated from the normalized spectra and the obtained multiplicities are listed in Table II. The intensities of the primary transitions to the

ground and the first excited states,  $I_0$  and  $I_1$ , are also listed. The ratio  $R_0$  defined as

$$R_0 = \frac{I_0}{I_0 + I_1}, \quad (2)$$

was also calculated and listed in Table II.

The pulse-height weighting technique [18] was employed to derive the neutron capture cross section. The averaged cross section over an energy bin,  $\langle\sigma\rangle$ , was obtained from the following equation [19]:

$$\langle\sigma\rangle = \frac{\sum_I W(I)S(I)}{(B_{ns} + \langle E_{n.c.m.} \rangle)N_s C_s \phi} - \frac{\sum_i (B_{ni} + \langle E_{n.c.m.} \rangle)N_i C_i \langle\sigma_i\rangle}{(B_{ns} + \langle E_{n.c.m.} \rangle)N_s C_s}, \quad (3)$$

TABLE II.  $\gamma$ -ray multiplicity of  $^{88}\text{Sr}(n, \gamma)^{89}\text{Sr}$  ( $>600$  keV), primary transition intensities of the ground and first excited states, and ground state transition ratio  $R_0 = I_0/(I_0 + I_1)$ .

Average neutron energy (Energy range) [keV]	Multiplicity ( $>600$ keV)			$R_0$
		$I_0$	$I_1$	$I_0/(I_0 + I_1)$
12 (10–14)	$2.2 \pm 0.2$	$0.03 \pm 0.01$	$0.50 \pm 0.02$	$0.052 \pm 0.011$
17 (14–19)	$2.4 \pm 0.7$	$0.11 \pm 0.04$	$0.21 \pm 0.04$	$0.34 \pm 0.03$
23 (19–26)	$2.3 \pm 0.3$	$0.19 \pm 0.02$	$0.14 \pm 0.02$	$0.57 \pm 0.01$
30 (26–34)	$2.2 \pm 0.2$	$0.16 \pm 0.01$	$0.08 \pm 0.01$	$0.66 \pm 0.09$
39 (34–44)	$2.6 \pm 0.3$	$0.10 \pm 0.01$	$0.07 \pm 0.01$	$0.75 \pm 0.01$
62 (44–89)	$2.2 \pm 0.2$	$0.19 \pm 0.01$	$0.07 \pm 0.01$	$0.73 \pm 0.01$
510 ( $\Delta E = 150$ )	$2.0 \pm 0.3$	$0.29 \pm 0.03$	$0.08 \pm 0.03$	$0.77 \pm 0.02$

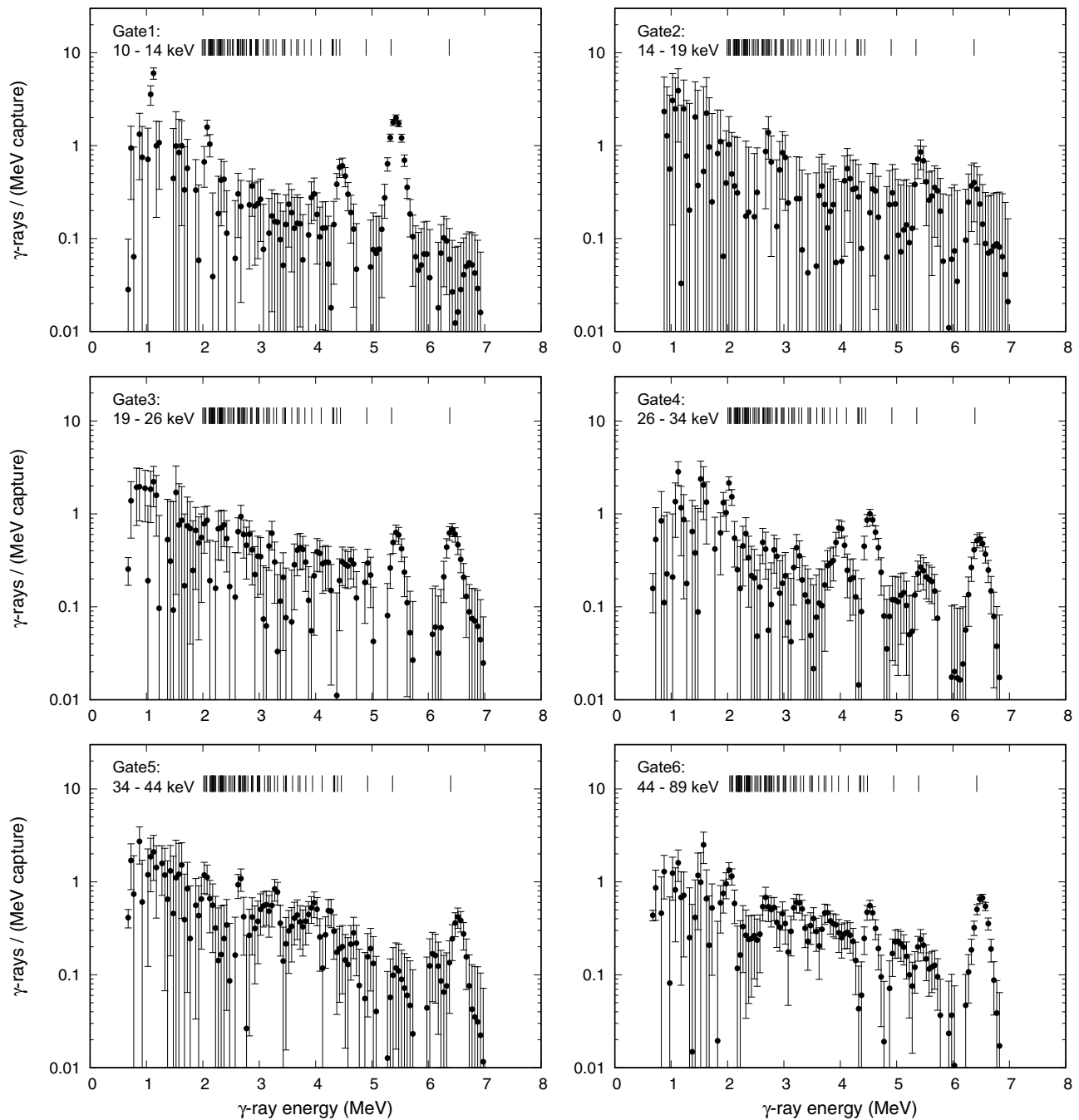


FIG. 5. Neutron capture  $\gamma$ -ray spectra of  $^{88}\text{Sr}$  in the low neutron energy region of 10–89 keV. The bars on top of the spectra indicate  $\gamma$ -ray energy positions of primary transitions from the neutron capture state to known discrete levels of  $^{89}\text{Sr}$ .

where  $S(I)$  is a PH spectrum of channel  $I$ ,  $W(I)$  is the weighting function,  $B_n$  is the neutron binding energy and  $\langle E_{n.c.m.} \rangle$  is the average neutron energy in the c.m. system. The second term is correction to remove contributions of sample constitute materials (carbon and oxygen of  $\text{SrCO}_3$  and the graphite sample container) and impurities in the samples. The suffixes  $s$  and  $i$  denote variables associated with the sample nuclide  $^{88}\text{Sr}$  and other nuclides, respectively. Neutron capture cross section data in JENDL-4.0 were used to calculate the average cross sections of sample constitute materials and impurities,  $\langle \sigma_i \rangle$ . Carbon, oxygen, and isotope

impurities  $^{87}\text{Sr}$  and  $^{86}\text{Sr}$  were taken into account. Contributions from other strontium isotopes and chemical impurities were negligible. The factor  $C$  is a neutron transport correction factor, including the self-shielding factor  $C_{ns}$  and the multiple scattering factor  $C_{nm}$  as  $C = C_{ns}C_{nm}$ . The factors  $C_{ns}$  and  $C_{nm}$  were calculated with the Monte Carlo simulation code TIM [20] and given in Table III. Absolute cross section values were determined from the relative ratio to the standard Au measurements. The  $^{197}\text{Au}(n, \gamma)^{198}\text{Au}$  cross section in ENDF/B-VII.1 was used as the standard cross section.

TABLE III. Neutron transport correction factors for the self-shielding  $C_{ns}$  and multiple scattering  $C_{nm}$  for samples, sample constitute materials carbon and oxygen, and isotope impurities.

Sample	Correction factor	Neutron energy region [keV]						
		10–14	14–19	19–26	26–34	34–44	44–89	510
$^{88}\text{Sr}$	$C_{ns}$	0.946	0.937	0.938	0.937	0.945	0.945	0.951
	$C_{nm}$	1.221	2.903	1.309	1.241	1.270	1.324	1.142
	$C = C_{ns} \cdot C_{nm}$	1.155	2.72	1.227	1.163	1.251	1.094	1.086
$^{87}\text{Sr}$	$C_{ns}$	0.946	0.940	0.942	0.943	0.945	0.946	0.951
	$C_{nm}$	1.370	1.291	1.407	1.228	1.175	1.158	1.157
	$C = C_{ns} \cdot C_{nm}$	1.295	1.213	1.326	1.158	1.110	1.096	1.100
$^{86}\text{Sr}$	$C_{ns}$	0.944	0.938	0.942	0.943	0.945	0.946	0.951
	$C_{nm}$	1.265	1.223	1.685	1.203	1.235	1.143	1.130
	$C = C_{ns} \cdot C_{nm}$	1.194	1.148	1.587	1.135	1.167	1.081	1.075
$^{16}\text{O}$	$C_{ns}$	0.945	0.940	0.942	0.943	0.945	0.946	0.945
	$C_{nm}$	1.440	1.332	1.296	1.239	1.200	1.125	1.180
	$C = C_{ns} \cdot C_{nm}$	1.361	1.252	1.222	1.169	1.134	1.065	1.115
$^{12}\text{C}$	$C_{ns}$	0.945	0.940	0.942	0.943	0.945	0.945	0.951
	$C_{nm}$	1.436	1.333	1.298	1.239	1.200	1.127	1.140
	$C = C_{ns} \cdot C_{nm}$	1.357	1.253	1.224	1.168	1.134	1.067	1.084
$^{197}\text{Au}$	$C_{ns}$	0.956	0.959	0.960	0.962	0.964	0.967	0.981
	$C_{nm}$	1.174	1.158	1.154	1.142	1.130	1.113	1.072
	$C = C_{ns} \cdot C_{nm}$	1.123	1.110	1.109	1.099	1.089	1.076	1.052

### III. RESULTS AND DISCUSSION

#### A. Neutron capture cross section

The obtained cross sections are summarized in Table IV. Statistical and systematic error components are listed in Table V. The systematic errors include uncertainties of the weighting function, the standard cross section of  $^{197}\text{Au}(n, \gamma)^{198}\text{Au}$ , cross section data for sample constitute materials and impurities, neutron transport correction factors, and estimation of undetected  $\gamma$ -ray contributions below a

threshold energy of 600 keV. Previous studies [21] estimated systematic errors of weighting functions at 4–6 %. However, the contribution of weighting functions to the overall cross section uncertainty is only around 1% because the sample and standard neutron capture yields were derived using the weighting functions calculated with the same method, which cancels out the systematic uncertainties in Eq. (3).

The results are plotted in Fig. 7. The evaluated cross sections of JENDL-4.0 [22] and ENDF/B-VII.1 are also plotted for comparison. The evaluated cross sections were averaged over the same energy bins as the present results below 89 keV, and 50-keV bin width above 89 keV. It is found that the present results and the evaluated cross sections are in good agreement in the low energy region up to 34 keV but both evaluations are by approximately 30% smaller than the present cross section in the energy range of 34–89 keV. At  $E_n = 510$  keV, the evaluated cross sections are based on statistical model

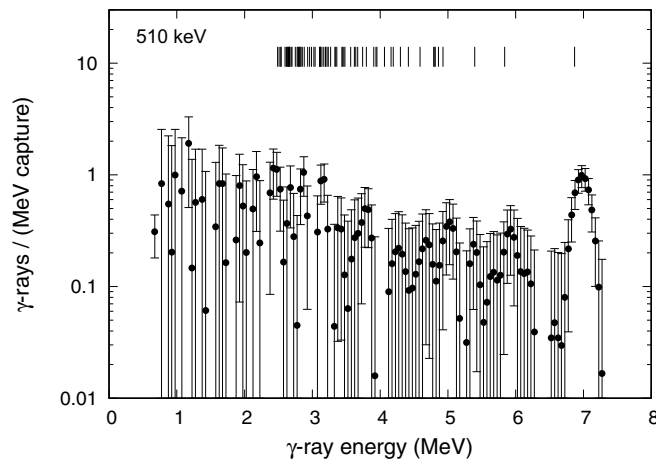


FIG. 6. Neutron capture  $\gamma$ -ray spectra of  $^{88}\text{Sr}$  at 510 keV. The bars on top of the spectra indicate  $\gamma$ -ray energy positions of primary transitions from the neutron capture state to known discrete levels of  $^{89}\text{Sr}$ .

TABLE IV. Neutron capture cross section of  $^{88}\text{Sr}$  in the present measurements.

Average neutron energy (Energy range) [keV]	Capture cross section [mb]
12 (10–14)	$36.6 \pm 2.5$ (6.9%)
17 (14–19)	$1.69 \pm 0.42$ (24.8%)
23 (19–26)	$8.12 \pm 0.65$ (8.0%)
30 (26–34)	$7.12 \pm 0.48$ (6.8%)
39 (34–44)	$3.24 \pm 0.28$ (8.6%)
62 (44–89)	$3.64 \pm 0.22$ (6.1%)
510 ( $\Delta E$ (FWHM) = 150)	$1.47 \pm 0.29$ (19.5%)



TABLE V. Statistical and systematic errors [%].

Error source	Neutron energy region [keV]						510
	10–14	14–19	19–26	26–34	34–44	44–89	
Statistics	4.9	23.5	6.0	4.5	6.5	3.3	16.6
Weighting function	1.0	1.0	1.0	1.0	1.0	1.0	1.0
Impurity correction	0.2	1.4	0.6	0.6	1.2	1.2	8.3
$^{197}\text{Au}(n, \gamma)$ cross section	3.0	3.0	3.0	3.0	3.0	3.0	3.0
Estimation of undetected $\gamma$ -ray contribution below 0.6 MeV							
$^{88}\text{Sr}$	0.7	1.1	1.2	0.9	1.7	1.5	2.0
$^{197}\text{Au}$	3.1	3.5	3.4	3.3	3.5	3.3	4.5
Self-shielding and multiple scattering							
$^{88}\text{Sr}$	1.3	6.3	1.9	1.4	2.0	0.9	0.8
$^{197}\text{Au}$	1.1	1.1	1.0	0.9	0.9	0.8	0.8
Total	6.9	24.8	8.0	6.8	8.6	6.1	19.5

calculations. JENDL-4.0 and the present data agree within the experimental uncertainty but the ENDF/B-VII.1 evaluation is by 50% larger than the present cross section.

The evaluated cross sections of  $^{88}\text{Sr}$  below 300 keV in both JENDL-4.0 and ENDF/B-VII.1 are based on the resonance parameters measured by Koehler *et al.* at ORELA [5,6]. The previous experimental results show that the  $p$ -wave resonances are dominant below 350 keV. Most of the  $p$ -wave resonance ( $IJ$ ) assignments in resonance analysis were far from satisfactory. Furthermore, even if the ( $IJ$ ) assignments are assumed correct, the  $\Delta_3$  test [23] indicates the existence of missing or misassignment of resonances above 75 keV for  $p_{1/2}$  resonances and 150 keV for  $p_{3/2}$  resonances. The disagreement between the present experimental data and the evaluated cross sections above 34 keV is consistent with the indication of missing resonances in the previous measurement.

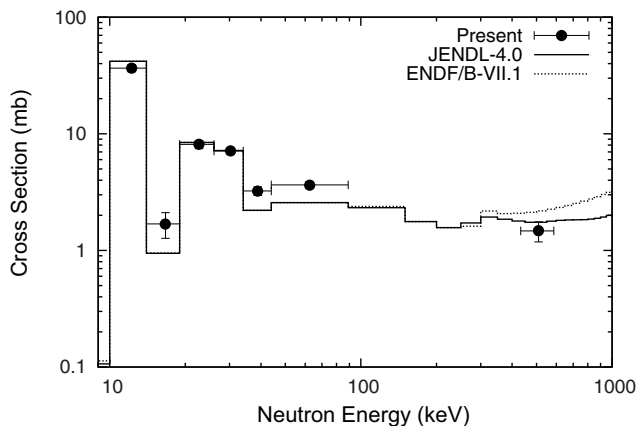


FIG. 7. Neutron capture cross section of  $^{88}\text{Sr}$ . The present results are shown as solid circles. Evaluated data of JENDL-4.0 and ENDF/B-VII.1 are shown for comparison. The evaluated cross sections are averaged over the same energy bins as the present experiments in the low energy region, and an energy bin of 50 keV in the high energy region.

### B. Maxwellian-averaged cross section

To investigate the impact of the present results on the stellar reaction rate, the MACS were calculated using the present cross sections. In addition to the present experimental data, the cross sections in the energy range above 89 keV were calculated using the statistical model. The statistical model calculation was made by the nuclear reaction model code CCONE [24]. The model parameters were first adjusted to reproduce the present cross section at  $E_n = 510$  keV, where the nuclear level density is expected to be large enough for the statistical model assumption. Then, the optimized parameters at 510 keV were used to calculate the cross sections between 89 keV and 510 keV. The cross section below 10 keV was adopted from JENDL-4.0. The cross sections for the MACS calculation are shown in Fig. 8.

One might consider that calculating the MACS using averaged cross sections over coarse energy bins could re-

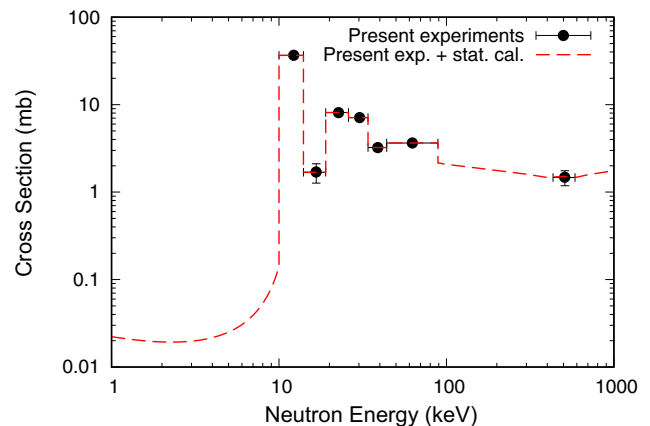


FIG. 8. Neutron capture cross section of  $^{88}\text{Sr}$  for Maxwellian-average calculation. The cross section consists of the present experimental data in 10–89 keV and theoretical model calculation in 89–510 keV. Theoretical model parameters are adjusted to reproduce the experimental cross section at 510 keV. The JENDL-4.0 cross section is adopted below 10 keV.

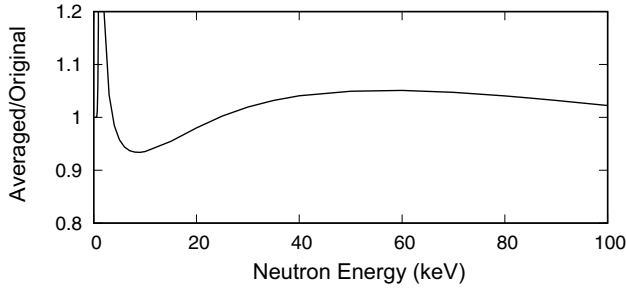


FIG. 9. Ratio of  $^{88}\text{Sr}$  MACS calculation using JENDL-4.0 cross section data averaged over the present energy bins to that using the original fine pointwise JENDL-4.0 data.

sult in significant differences compared to calculations using fine energy grids. To assess the impact of this coarse cross section binning, we compared the MACS calculations using JENDL-4.0 cross section data averaged over the current energy bins with the original fine-pointwise cross section. Figure 9 illustrates the ratio of MACS obtained from the averaged cross section to the MACS derived from the original JENDL-4.0 data. In general, the ratio remains below 5% except for the low energy region ( $E_n < 15$  keV). This effect proves to be smaller than the observed discrepancy between the present and previous MACS results.

The present MACS calculation results are shown in Table VI and plotted in Fig. 10. The given uncertainties were calculated from uncertainties of the present experimental cross sections. The contributions from the experimental data ( $E_n < 89$  keV) and the statistical model calculations ( $E_n > 89$  keV) are also shown. The contribution from the cross section below 10 keV is very small. The MACS values given in

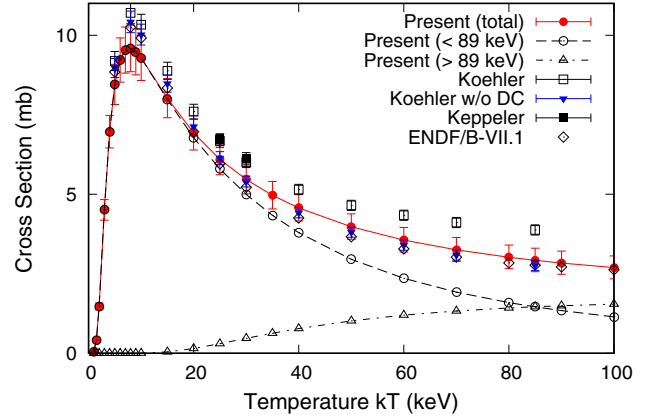


FIG. 10. Maxwellian-averaged neutron capture cross section of  $^{88}\text{Sr}$  calculated from the present cross section depicted in Fig. 8. Contributions from the experimental data ( $E_n < 89$  keV) and theoretical calculation ( $E_n > 89$  keV) are also plotted. Previous works by Koehler *et al.* [5] and Käppeler *et al.* [8], and MACS obtained from ENDF/B-VII.1 are plotted for comparison. For the MACS of Ref. [5], data both with and without the direct capture (DC) contribution are plotted.

Refs. [5] and [8] are listed for comparison. Koehler *et al.* calculated the MACS from their resonance parameters and added the theoretically calculated direct capture (DC) contribution, which is a nonresonant process and cannot be detected by the resonance analysis method [5,6]. Table VI and Fig. 10 show the calculation in Refs. [5,6] both with and without the DC contribution. The MACS of Refs. [5,6] are approximately 10% larger than the present results over the whole energy range but the agreement is improved when the DC

TABLE VI. Maxwellian-averaged neutron capture cross sections (MACS) calculated from the present experimental cross sections and theoretical model calculation. Contributions from the experimental data ( $E_n < 89$  keV) and theoretical calculation ( $E_n > 89$  keV) are also shown. MACS data by Koehler *et al.* [5], Käppeler *et al.* [8], and ENDF/B-VII.1 are listed for comparison. Reference [5] gave MACS calculated from their resonance experimental data and added direct capture contribution (+DC).

$kT$ [keV]	Maxwellian-averaged cross section $\langle\sigma\rangle$ [mb]						
	Total	Present		Koehler <i>et al.</i> [5]		Käppeler <i>et al.</i> [8]	ENDF/B-VII.1
		$E_n < 89$ keV	$E_n > 89$ keV	Resonances	+DC		
5	$8.45 \pm 0.63$	8.45	$1 \times 10^{-6}$	8.97	$9.19 \pm 0.30$		8.84
8	$9.58 \pm 0.73$	9.58	$5 \times 10^{-3}$	10.42	$10.70 \pm 0.34$		10.3
10	$9.29 \pm 0.71$	9.28	$3 \times 10^{-3}$	10.02	$10.33 \pm 0.33$		9.91
15	$8.02 \pm 0.61$	7.98	0.05	8.48	$8.88 \pm 0.27$		8.34
20	$6.93 \pm 0.53$	6.78	0.15	7.13	$7.60 \pm 0.23$		6.97
25	$6.10 \pm 0.48$	5.80	0.30	6.14	$6.68 \pm 0.20$	$6.72 \pm 0.18$	5.96
30	$5.46 \pm 0.45$	4.99	0.47	5.40	$6.01 \pm 0.17$	$6.13 \pm 0.18$	5.22
40	$4.57 \pm 0.42$	3.79	0.78	4.42	$5.15 \pm 0.16$		4.25
50	$3.98 \pm 0.40$	2.96	1.02	3.81	$4.65 \pm 0.16$		3.66
60	$3.56 \pm 0.40$	2.36	1.20	3.40	$4.34 \pm 0.16$		3.28
70	$3.25 \pm 0.39$	1.92	1.33	3.09	$4.11 \pm 0.16$		3.02
80	$3.02 \pm 0.38$	1.59	1.43				2.84
85	$2.92 \pm 0.38$	1.46	1.46	2.76	$3.88 \pm 0.16$		2.77
90	$2.84 \pm 0.36$	1.34	1.50				2.72
100	$2.69 \pm 0.35$	1.14	1.55				2.63



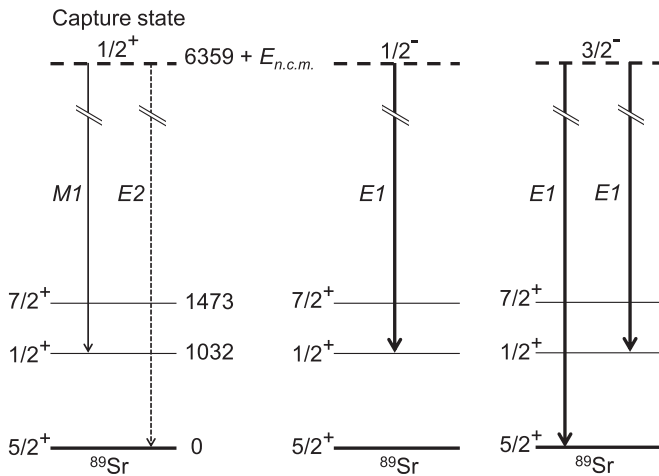


FIG. 11. Level scheme of  $^{89}\text{Sr}$ . Allowed dominant electromagnetic transitions ( $E1$ ,  $E2$ , and  $M1$ ) from different  $J^\pi$  neutron capture states ( $\frac{1}{2}^+$ ,  $\frac{1}{2}^-$ , and  $\frac{3}{2}^-$ ) to the ground ( $\frac{5}{2}^+$ ), first ( $\frac{1}{2}^+$ , 1032 keV), and second ( $\frac{7}{2}^+$ , 1473 keV) excited states are shown.

contribution is not included. The DC cross section might be overestimated in the theoretical calculation.

### C. Neutron capture $\gamma$ -ray spectrum

The present experimental results show that the neutron capture  $\gamma$ -ray spectrum of  $^{88}\text{Sr}$  drastically changes with the incident neutron energy as shown in Fig. 5. In the lowest neutron energy gate of 10–14 keV (Gate 1), the primary transition to the first excited state ( $E_x = 1032$  keV) was clearly observed but the transition to the ground state was not. With the neutron energy increasing, the peak of the ground state transition appears and the transition to the first excited state becomes weaker. Transition probabilities from a neutron capture state to lower energy levels are strongly governed by the selection rules of electromagnetic transition. The  $J^\pi$  values of the ground and first excited states of  $^{89}\text{Sr}$  are  $\frac{5}{2}^+$  and  $\frac{1}{2}^+$ , respectively. This large spin difference makes difference of intensities between the two primary  $\gamma$  rays. In addition, possible  $J^\pi$  values of the capture state are limited by the incident neutron orbital angular momentum  $l$ . The  $s$ - and  $p$ -wave resonances are dominant in this energy region. The  $s$ -wave neutron resonance forms a  $^{89}\text{Sr}$  capture state in  $J^\pi = \frac{1}{2}^+$ . The  $p$ -wave resonances ( $p_{1/2}$  and  $p_{3/2}$ ) lead to  $\frac{1}{2}^-$  and  $\frac{3}{2}^-$ . Figure 11 shows level schemes of low-lying levels of  $^{89}\text{Sr}$  and transitions from different  $J^\pi$  capture states. The most dominant electromagnetic transition  $E1$  is forbidden for decay from the  $\frac{1}{2}^+$  state to the low-lying states. Higher multipolarity transitions  $E2$  or  $M1$  that are much weaker than  $E1$  are required. On the other hand, the  $E1$  transition is allowed in  $\frac{1}{2}^- \rightarrow 1\text{st}(\frac{1}{2}^+)$ ,  $\frac{3}{2}^- \rightarrow \text{gnd}(\frac{5}{2}^+)$  and  $\frac{3}{2}^- \rightarrow 1\text{st}(\frac{1}{2}^+)$ . Accordingly, primary  $\gamma$ -ray intensities to the ground and first excited states can change with resonance  $lJ$  values. The resonance distribution of  $^{88}\text{Sr}$  is very sparse in the present energy range. Only a small number of resonances contribute to the neutron capture reaction in one energy gate. Contributions

from  $s_{1/2}$ ,  $p_{1/2}$ , and  $p_{3/2}$  resonances significantly fluctuate with the neutron energy. The observed difference of the  $\gamma$ -ray spectrum between neutron energy gates can be interpreted as results of the resonance effect. In fact, according to JENDL-4.0, the energy region Gate 1 includes two major resonances,  $p_{1/2}$  at 12.4 keV and  $s_{1/2}$  at 13.8 keV. The  $p_{1/2}$  and  $s_{1/2}$  capture states do not decay to the  $\frac{5}{2}^+$  ground state via the  $E1$  transition. Only the  $p_{1/2}$  capture state can decay to the first excited state. This is consistent with the experimental result that the prompt  $\gamma$  ray of transition of the first excited state but not the ground state was observed in Gate 1.

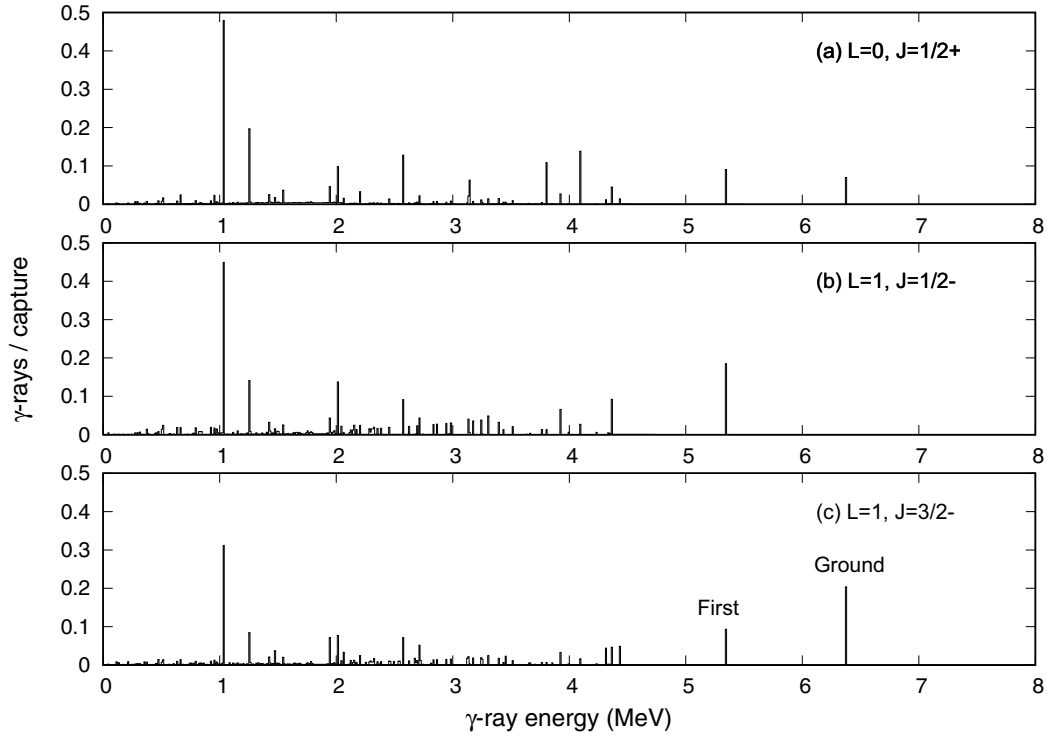
For more quantitative discussion, neutron capture  $\gamma$ -ray spectra from different  $J^\pi$  channels were calculated using the statistical Hauser-Feshbach code CoH3 [25]. Calculation is decomposed to different channels denoted by the  $(lJ)$  values. The calculated  $\gamma$ -ray energy spectra are shown in Fig. 12. The  $\gamma$ -ray spectra are normalized by Eq. (1). The calculated spectra shown in Fig. 12 are for the incident neutron energy of 12 keV but the shape of each decomposed  $\gamma$ -ray spectrum is almost insensitive to the neutron energy in the present energy range. The peak intensities of the ground and first excited state transitions,  $I_0$  and  $I_1$ , were derived from the spectrum of each  $(lJ)$  channel. The ground state transition ratio  $R_0$  defined in Eq. (2) was also calculated from  $I_0$  and  $I_1$ . The obtained  $I_0$ ,  $I_1$ , and  $R_0$  values are shown in Table VII. The  $R_0$  values are consistent with the selection rules of electromagnetic transitions qualitatively discussed above.

The partial cross sections of the  $s_{1/2}$ ,  $p_{1/2}$ , and  $p_{3/2}$  channels were derived using the resonance parameters in JENDL-4.0. The partial cross sections  $\sigma_{s_{1/2}}$ ,  $\sigma_{p_{1/2}}$ , and  $\sigma_{p_{3/2}}$  were averaged within a certain energy interval to facilitate our data analysis. The calculated averaged cross sections are shown in Fig. 13. Multiplying the partial cross section with the  $I_0$  and  $I_1$  values of the corresponding channel denoted by the suffices  $s_{1/2}$ ,  $p_{1/2}$ , and  $p_{3/2}$ , the average  $I_0$  and  $I_1$  values were calculated as the following equations:

$$I_0 = \sigma_{s_{1/2}} I_{0,s_{1/2}} + \sigma_{p_{1/2}} I_{0,p_{1/2}} + \sigma_{p_{3/2}} I_{0,p_{3/2}},$$

$$I_1 = \sigma_{s_{1/2}} I_{1,s_{1/2}} + \sigma_{p_{1/2}} I_{1,p_{1/2}} + \sigma_{p_{3/2}} I_{1,p_{3/2}}.$$

The  $R_0$  ratio was calculated from the average  $I_0$  and  $I_1$  values in each energy bin. The calculated  $R_0$  values are plotted in Fig. 14, compared with the present experimental data listed in Table II. The theoretical calculation is in good agreement with experimental results up to the neutron energy of 34 keV but deviates from the experimental values in the higher energy region. The origin of the disagreement is not clear but above 34 keV, deviation of the evaluated cross section from the present experimental data was also seen in Fig. 7. This indicates that the disagreement of  $R_0$  may be caused by missing or  $(lJ)$  misassignment of resonances in the previous resonance measurement, which the evaluated cross section data are based on. To increase the theoretical  $R_0$  value, more  $p_{3/2}$  resonances are required, while no  $p_{3/2}$  resonances were assigned in the previous resonance analysis in Gate 5 (34–44 keV). The  $\gamma$ -ray spectra give more indication of possible  $(lJ)$  misassignment. For example, the experimental  $\gamma$ -ray spectrum in Gate 4 shows two  $\gamma$ -ray peaks around 4 MeV in addition to  $\gamma$ -ray peaks of the ground and first excited states. This pattern is very

FIG. 12. Calculated  $\gamma$ -ray spectra from different capture spin states.

similar to the theoretical  $\gamma$ -ray spectrum from the  $s_{1/2}$  state in Fig. 12 but no  $s_{1/2}$  resonance is reported in the energy region as shown in Table I. To solve the observed discrepancies of the cross section and  $\gamma$ -ray spectrum, further theoretical and experimental studies are necessary.

#### IV. CONCLUSION

The neutron capture cross section and the capture  $\gamma$ -ray spectrum of  $^{88}\text{Sr}$  were measured in two keV-energy regions: 10–89 keV and 510 keV. The incident neutron energy was determined by the time-of-flight method and neutron capture  $\gamma$  rays were detected with a heavily shielded NaI(Tl) spectrometer. The experimental results agree with evaluated cross sections of JENDL-4.0 and ENDF/B-VII.1 up to 34 keV but disagree at higher energies. Both the JENDL-4.0 and ENDF/B-VII.1 evaluations are 30% smaller than the present

results in the energy range of 34 to 89 keV. The disagreement can be interpreted as missing of resonances in the previous resonance measurement which has been already pointed out in Ref. [6]. In addition, we calculated the Maxwellian-averaged neutron capture cross sections using the present experimental cross section. The lack of the cross section in the energy range that the present experiment does not cover was compensated by a statistical nuclear reaction model calculation. The calculated MACS resulted in about 10% smaller values than those given in Ref. [6], which were based on the resonance measurements and additional direct capture cross section estimated by a theoretical model. It is found that the difference between the present and previous MACS almost disappears when the direct capture contribution is removed from the previous MACS. Hence, the direct capture cross section was probably overestimated in the calculation. The neutron capture  $\gamma$ -ray spectrum demonstrated strong neutron energy dependence. The primary

TABLE VII. Primary transition intensities of the ground and first excited states,  $I_0$  and  $I_1$ . Ground state transition ratio  $R_0 = I_0/(I_0 + I_1)$ .

$E_n$ [keV]	$s_{1/2}$			$p_{1/2}$			$p_{3/2}$		
	$I_0$	$I_1$	$R_0$	$I_0$	$I_1$	$R_0$	$I_0$	$I_1$	$R_0$
12	0.070	0.093	0.43	$9.0 \times 10^{-5}$	0.19	$4.8 \times 10^{-4}$	0.20	0.095	0.68
17	0.070	0.093	0.43	$9.0 \times 10^{-5}$	0.19	$4.8 \times 10^{-4}$	0.20	0.095	0.68
23	0.070	0.093	0.43	$9.0 \times 10^{-5}$	0.19	$4.8 \times 10^{-4}$	0.20	0.095	0.68
30	0.069	0.093	0.43	$8.9 \times 10^{-5}$	0.19	$4.8 \times 10^{-4}$	0.20	0.095	0.68
39	0.069	0.092	0.43	$8.9 \times 10^{-5}$	0.19	$4.8 \times 10^{-4}$	0.20	0.095	0.68
62	0.068	0.091	0.43	$8.8 \times 10^{-5}$	0.19	$4.7 \times 10^{-4}$	0.20	0.094	0.68

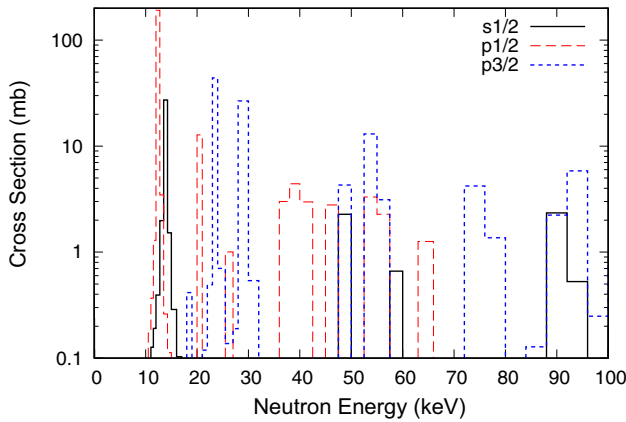


FIG. 13. Calculated resonance spin components of capture cross section of  $^{88}\text{Sr}$ .

transition to the  $\frac{5}{2}^+$  ground state of  $^{89}\text{Sr}$  was not observed in the lowest energy bin of 10–14 keV while the transition to the first excited state of  $\frac{1}{2}^+$  was clearly observed. However going to higher energy, the ground state transition appears and becomes strong. The experimental ground state transition ratio was compared with estimation calculated from the  $(I, J)$  partial cross sections derived from the resonance parameters in JENDL-4.0 and prompt  $\gamma$ -ray spectra from the  $(I, J)$  capture states calculated with a statistical nuclear reaction model. The experimental results and calculation agrees up to 34 keV but calculated value significantly deviates above 34 keV. The

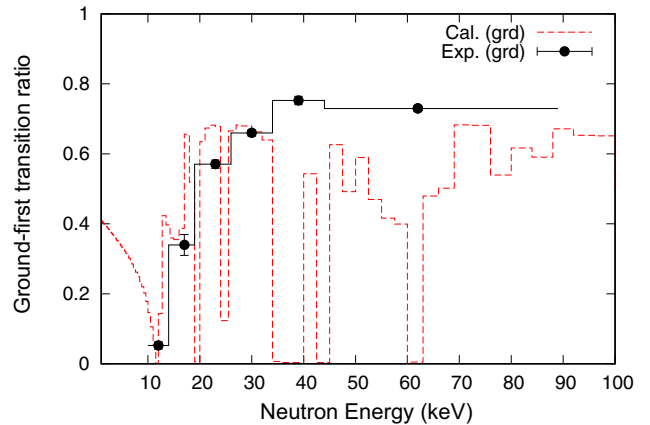


FIG. 14. Ground-first transition ratio. The theoretically calculated transition ratio is compared with the experimental values.

disagreement could be caused by missing or  $(I, J)$  misassignment of resonances in the previous resonance measurement.

#### ACKNOWLEDGMENTS

This work was supported by the Tokyo Tech World Research Hub Initiative (WRHI), Program of the Institute of Innovative Research, Tokyo Institute of Technology. To.K. performed this work under the auspices of the National Nuclear Security Administration of the U.S. Department of Energy at Los Alamos National Laboratory under Contract No. 89233218CNA000001.

- [1] F. Käppeler, R. Gallino, S. Bisterzo, and W. Aoki, *Rev. Mod. Phys.* **83**, 157 (2011).
- [2] C. M. Raiteri, M. Busso, R. Gallino, and G. Picchio, *Astrophys. J.* **371**, 665 (1991).
- [3] M. Limongi, O. Straniero, and A. Chieffi, *Astrophys. J. Suppl. Ser.* **129**, 625 (2000).
- [4] M. Pignatari, R. Gallino, M. Heil, M. Wiescher, F. Käppeler, F. Herwig, and S. Bisterzo, *Astrophys. J.* **710**, 1557 (2010).
- [5] P. E. Koehler, R. R. Winters, K. H. Guber, T. Rauscher, J. A. Harvey, S. Raman, R. R. Spencer, J. C. Blackmon, D. C. Larson, D. W. Bardayan, and T. A. Lewis, *Phys. Rev. C* **62**, 055803 (2000).
- [6] P. E. Koehler, R. R. Winters, K. H. Guber, T. Rauscher, J. A. Harvey, S. Raman, R. R. Spencer, J. C. Blackmon, D. C. Larson, D. W. Bardayan, and T. A. Lewis, *Phys. Rev. C* **63**, 049901(E) (2001).
- [7] J. Boldeman, B. Allen, A. de L. Musgrove, R. Macklin, and R. Winters, *Nucl. Phys. A* **269**, 397 (1976).
- [8] F. Käppeler, W. R. Zhao, H. Beer, and U. Ratzel, *Astrophys. J.* **355**, 348 (1990).
- [9] M. Chadwick, M. Herman, P. Obložinský, M. Dunn, Y. Danon, A. Kahler, D. Smith, B. Pritychenko, G. Arbanas, R. Arcilla, R. Brewer, D. Brown, R. Capote, A. Carlson, Y. Cho, H. Derrien, K. Guber, G. Hale, S. Hoblit, S. Holloway *et al.*, *Nucl. Data Sheets* **112**, 2887 (2011).
- [10] K. Shibata, O. Iwamoto, T. Nakagawa, N. Iwamoto, A. Ichihara, S. Kunieda, S. Chiba, K. Furutaka, N. Otuka, T. Ohsawa, T. Murata, H. Matsunobu, A. Zukeran, S. Kamada, and J. Katakura, *J. Nucl. Sci. Technol.* **48**, 1 (2011).
- [11] *Compendium of Neutron Beam Facilities for High Precision Nuclear Data Measurements. Annex: Individual Reports*, TECDOC Series No. 1743 (International Atomic Energy Agency, Vienna, 2014).
- [12] T. Katabuchi, N. C. Hai, M. Igashira, S. Kamada, M. Tajika, and M. Mizumoto, *J. Korean Phys. Soc.* **59**, 1844 (2011).
- [13] M. Igashira, H. Kitazawa, and N. Yamamuro, *Nucl. Instrum. Methods Phys. Res. A* **245**, 432 (1986).
- [14] S. Mizuno, M. Igashira, and K. Masuda, *J. Nucl. Sci. Technol.* **36**, 493 (1999).
- [15] S. F. Mughabghab, *Atlas of Neutron Resonances, Resonance Parameters and Thermal Cross Sections, Z=1–100* (Elsevier, Amsterdam, 2006).
- [16] H. Kendrick and S. M. Speering, *An Introduction to the Principles and Use of the FERDOR Unfolding Code*, Technical Report No. GA-9882 (General Atomics, San Diego, 1970).
- [17] R. Capote, M. Herman, P. Obložinský, P. G. Young, S. Goriely, T. Belgia, A. V. Ignatyuk, A. J. Koning, S. Hilaire, V. A. Plujko, M. Avrigeanu, O. Bersillon, M. B. Chadwick, T. Fukahori, Z. Ge, Y. Han, S. Kailas, J. Kopecky, V. M. Maslov, G. Reffo *et al.*, *Nucl. Data Sheets* **110**, 3107 (2009).
- [18] R. L. Macklin and J. H. Gibbons, *Phys. Rev.* **159**, 1007 (1967).

- [19] T. Katabuchi, M. Igashira, and Y. Kiyonagi, *J. Nucl. Sci. Technol.* **48**, 744 (2011).
- [20] K. Senoo, Y. Nagai, T. Shima, T. Ohsaki, and M. Igashira, *Nucl. Instrum. Methods Phys. Res. A* **339**, 556 (1994).
- [21] J. Nishiyama, M. Igashira, T. Ohsaki, G. Kim, W.-C. Chung, and T.-I. Ro, *J. Nucl. Sci. Technol.* **45**, 352 (2008).
- [22] K. Shibata, A. Ichihara, and S. Kunieda, *J. Nucl. Sci. Technol.* **47**, 1055 (2010).
- [23] F. J. Dyson and M. L. Mehta, *J. Math. Phys.* **4**, 701 (1963).
- [24] O. Iwamoto, *J. Nucl. Sci. Technol.* **44**, 687 (2007).
- [25] T. Kawano, R. Capote, S. Hilaire, and P. Chau Huu-Tai, *Phys. Rev. C* **94**, 014612 (2016).